Formation, propagation, reflection, and collision of microwave envelope solitons in yttrium iron garnet films

N. G. Kovshikov and B. A. Kalinikos
St. Petersburg Electrotechnical University, 197376, St. Petersburg, Russia

C. E. Patton, E. S. Wright, and J. M. Nash
Department of Physics, Colorado State University, Fort Collins, Colorado 80523

(Received 10 April 1996)

The end edge reflection and collision of backward volume wave bright microwave magnetic envelope solitons in long and narrow yttrium iron garnet single-crystal films has been studied experimentally. The experiments were done on 5.1-μm-thick, 1-mm-wide films. The bright solitons were excited by single or double 8–36-ns-wide microwave pulses with a nominal carrier frequency of 5.8 GHz. The experiments utilized a movable transducer structure to make measurements for a range of transducer separations from 2 to 15 mm and for pulses before and after reflection. The soliton character was established from single-pulse decay versus time and distance measurements. Three decay regions were observed, a slow decay region before soliton formation, a fast decay region characteristic of solitons, and a second slow decay for linear pulses. The soliton region included both incident and reflected pulses. The exponential decay rate for the soliton regime was greater than for the linear. The soliton pulses retained the same shape and speed after edge reflection. An observed drop in pulse amplitude after passing under the pickup transducer provided a way to measure the actual power and amplitude of the soliton signal. The measured amplitudes and widths were in fair agreement with predictions for a simple sech-type order one soliton pulse. For properly timed double-pulse experiments in which a reflected lead pulse collides with the follow-on pulse before detection, the effects of soliton collisions could be examined. In the single soliton power regime, the pulses were found to retain their shape and speed after collision. At higher powers, shapes were not retained. In addition, a wake effect was observed in which the lead pulse causes a change in the detected signal for the follow-on pulse, even without collision. [S0163-1829(96)00845-4]

I. INTRODUCTION

The term ''soliton'' usually refers to a propagating nonlinear pulse or wave packet which preserves its shape without dispersive spreading. In the past three decades, soliton excitations have been realized in many physical systems.[1–3] One well-known example is that of optical envelope solitons in fibers.[4] In recent years, new work has been done on microwave magnetic envelope (MME) solitons in thin films. This work has included studies of both dipole-exchange forward volume wave (FVW) solitons,[5–7] magnetostatic backward volume wave (BVW) solitons,[8] and magnetostatic surface wave solitons.[9,10] These experimental results have been discussed in qualitative terms based on the balance between nonlinear effects and dispersion, and quantitatively in terms of the nonlinear Schrödinger equation.

One of the established defining features of a soliton, in addition to propagation without spreading, is in its ability to collide with another similar soliton and emerge after the collision with an unchanged shape and speed. In the case of MME solitons, such collision experiments have only been reported for the forward volume wave case indicated above.[7,11] These experiments were carried out by (1) propagating two FVW soliton pulses along a long and narrow YIG film, and (2) setting up conditions for collision by allowing the first pulse to be reflected from the end edge of the film and then collide with the still approaching second soliton pulse. It was found that reflection at the end of the film occurred with only minimal loss, below 0.1 dB, and that the two FVW solitons could pass through each other without changing their shapes.

This paper reports the results of reflection and collision experiments for backward volume wave solitons. In addition to the basic confirmation of shape and speed preservation after collision, these reflection and collision experiments reveal several particularly new results as well. First, the reflection measurements provide a way to determine the actual spin-wave power carried by the propagating MME pulse as it passes under the pick-up strip line transducer and transfers a measurable fraction of that power to the pickup line. Second, the pulse power measurements as a function of the pickup transducer position exhibit decay properties which allow one to identify specific propagation regions along the YIG strip for soliton formation, soliton propagation, and linear MME pulse propagation. Third, the measured profiles for the double-pulse propagation experiments show a wake effect at powers above the single soliton range, in which the passage of the first forward traveling pulse perturbs the YIG film in some way which significantly affects the observed properties of the second forward traveling pulse. Moreover, upon reflection of the first pulse and collision with the still forward traveling second pulse, there exists a regime of power above the single soliton regime for which the interaction causes significant changes in the overall profiles.

The organization of this paper is as follows: Section II provides a summary of the experiment and the basic magne-

tostatic backward volume wave parameters which are applicable to the measurements and the data analysis. Section III presents the results of the single-pulse reflection experiments and provides a brief analysis of those results. Section IV presents the results of the two-pulse experiments and a qualitative discussion of these results.

II. EXPERIMENT AND NOMENCLATURE

The starting point for linear MME pulses and solitons in magnetic thin films is with the magnetostatic waves first discussed by Damon and Eshbach.[12] These MME pulses are typically generated and detected by microstrip antennas and propagated between antennas with characteristic group velocities, dispersion effects, and decay properties which follow established principles. The backward volume wave solitons considered here derive from magnetostatic backward volume wave packets at high power. This section provides a brief overview of (a) the experimental techniques used for the measurement of such excitations and (b) selected theoretical considerations needed to interpret and analyze the experiments. Detailed descriptions in both areas can be found in Refs. 7 and 8.

A. Experiment

The measurements utilized several epitaxial YIG films and a special planar microwave transducer structure for which the pickup antenna could be moved and positioned accurately relative to the input antenna while maintaining the film strip in a fixed position relative to the input antenna. As will be evident shortly, this capability to accurately position the pickup antenna relative to both the input antenna and the film edge used for reflection was critical to the measurement results. This structure will be discussed shortly.

Several different films were used for the experiments. The films were grown on a (111) plane single-crystal gadolinium gallium garnet (GGG) substrate by the method of liquid phase epitaxy (LPE). The films used in this work had unpinned surface spins and the excitations generated in the experiments were taken to be purely dipolar spin waves or magnetostatic waves.[13] The films had narrow ferromagnetic resonance linewidths, typically in the 0.5 Oe range at 10 GHz. They exhibited properties generally associated with films with no appreciable surface spin-pinning effects. That is, the ferromagnetic resonance spectra exhibited no pronounced spin-wave resonance peaks and the magnetostatic surface wave and forward volume wave transmission profiles showed no pronounced notches usually associated with pinning. The results presented in this report are for one film sample of thickness 5.1 μm, as determined from the LPE processing parameters and by optical methods.

The film featured below was carefully cut into a long and narrow rectangular strip with a width W of 1.0 mm and a length of 40 mm. The narrow width served to reduce possible transverse instability and diffraction effects. Care was taken to properly prepare the short edges at the ends of the YIG strip. The short edge intended for reflection was cut to be perpendicular to the axis of the strip. The other short edge was tapered to reduce unwanted reflections.

For the microwave measurements, the film strip was positioned, with the YIG side down and GGG substrate side up, over the microwave transducer and mechanical stage as depicted schematically in Fig. 1. Figure 1(a) shows the grounded input and pickup microstrip transducer lines on two separate copper clad microwave dielectric substrate structures. The mechanical stage was designed to allow for the translation of the pickup antenna along the long dimension of the YIG strip. The input and output microstrip lines were designed for an impedance of 50Ω, with narrower 50-μm-wide, 2-mm-long sections just under the YIG film portions. These 50-μm-wide sections under the YIG were needed for efficient wide band excitation and detection of the magnetostatic wave pulses for the operating point and pulse widths of the experiment. Figure 1(a) also shows a vector **H** which is parallel to the long direction of the YIG strip. This **H** denotes the static magnetic field. A field parallel to the propagation direction down the YIG strip from the input antenna to the pickup antenna and far edge of the YIG results in magnetostatic backward volume wave signal propagation.

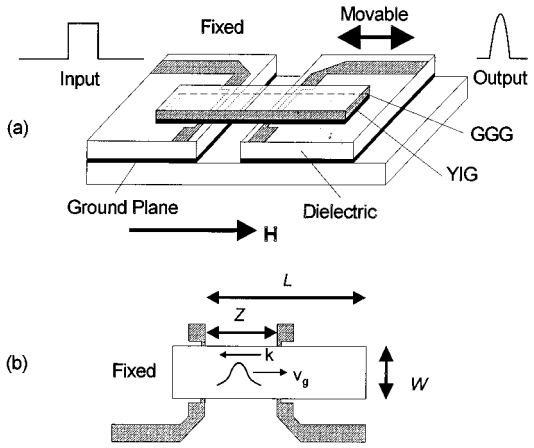

FIG. 1. (a) Schematic diagram of the YIG film transducer structure. (b) Propagation geometry and spacings for the film strip and the movable transducer section. The structure consists of two separate planar microstrip transmission line sections which narrow down to input and output transducer sections. These lines are on the top surfaces of microwave dielectric substrates with conducting ground plane backings. The long and narrow YIG film on a gadolinium gallium garnet (GGG) substrate is positioned YIG side down over the transducer sections of the input and output microstrip lines. The input line section is fixed in position and the output section is movable. The distance from the input transducer to the far edge of the film is denoted as L. The distance from the input transducer to the movable output transducer is denoted as Z. The structure supports the propagation of BVW pulses with a carrier signal wave vector **k** and a group velocity $\mathbf{v}_g$.

Figure 1(b) shows the YIG film strip and the two antennas across the film in simplified schematic form to define clearly the geometry and the mechanical positioning parameters for the experiments. The diagram also shows a pulse propagating at some carrier wave vector **k** and group velocity $\mathbf{v}_g$. For BVW excitations, **k** and $\mathbf{v}_g$ are oppositely directed. The distance between the input microstrip antenna and the far end edge of the YIG film is designated as L. For the various sequences of measurements to be presented below, this distance was maintained at fixed values in the 8–10 mm range. The distance between the input microstrip antenna and the output antenna is designated as Z in Fig. 1(b). In the experi-

ments, this distance was changed by moving the pickup transducer under the YIG film. The mechanical stage range of movement allowed Z to be varied between 2 and 15 mm. The accurate determination of these distances will be particularly critical to the analysis of the pulse reflection data. They were determined through visual measurement of actual distances with a traveling microscope in combination with a vernier scale on the translation stage, and by extrapolation from the actual pulse timing versus position data. The visual measurements were accurate to about 0.1 mm. The single-pulse data to be presented in Sec. III also indicate a position error from the pulse timing data in the ± 0.1 mm range.

Three specific measurements form the basis of the results to be presented below. These are (1) measurements of cw transmitted power versus frequency under low power conditions, (2) measurements of peak powers for the detected pulses at the output antenna as a function of the antenna position Z for different input pulse powers, and (3) measurements of the actual profiles of the various pulse signals at the output antenna. The control parameters for such experiments are, of course, the geometry, the microwave carrier frequency f, the value H of the static field, the microwave input pulse width T_o, and the input pulse peak power P_{in}. For cw signals or pulse widths which are not too narrow, that is, when $T_o \gg 1/f$ is satisfied, the choices of geometry, frequency, and field determine the carrier wave number k and the group velocity $\mathbf{v}_g$, as well as other parameters related to the dispersive and nonlinear effects. With ω and k specified, the choices for T_o and P_{in} further determine the actual dispersive and nonlinear response properties for the experimental pulses. These parameters will be considered in more detail shortly.

The input microwave signals, both pulse and cw, were obtained from a Hewlett-Packard synthesized sweeper, a fast pulse generator, a fast microwave switch, and a power amplifier. Microwave pulses with widths as narrow as 3 ns were possible. The results presented below are for an input pulse width of 24 ns, as measured at the half power positions on the pulse profile. The input and output microwave signals were detected and analyzed with the aid of a Hewlett-Packard microwave transition analyzer (MTA). The MTA could be operated in either the frequency domain as a network analyzer or in the time domain as a fast sampling digital oscilloscope. Measurements in the frequency domain were used to characterize the transmission properties of the MSW signal. Pulse measurements in the time domain were used to obtain most of the data to be considered shortly. The static magnetic field was provided by a conventional iron yoke electromagnet and measured with a digital Hall effect gaussmeter. The entire system was controlled from a personal computer through a standard IEEE-488 interface bus. Further details on the basic setup of the experiments may be found in Refs. 2 and 3.

A directional coupler was used to sample the microwave signal applied to the input transducer. With cable and connector loss taken into account, the input signal as detected at the MTA was approximately 27 dB down from the signal at the input transducer shown in Fig. 1. Measurements of incident and reflected power at the input connection to the transducer structure yielded a power coupling efficiency of approximately 0.20 at the operating point for the MSW measurements. That is, approximately 20% of the incident power was converted into MSW pulse power in the YIG.

The output signal level at the MTA was approximately 2 dB down from the signal at the output transducer. The combination of measurements on forward traveling pulses and pulses traveling in the reverse direction after reflection made it possible to extrapolate backward from the MTA signal to determine the actual spin-wave power at the pickup strip line. This capability will be critical for the data analysis at the end of Sec. III. As will be shown, the MSW power conversion efficiency to strip line power was approximately 25%.

In the results presented below, signal levels are given in several ways. The input power levels shown on the left side vertical axes for the pulse signals in Figs. 3 and 8 are indicated in mW. These values correspond to the actual power levels detected at the input channel to the microwave transition analyzer (MTA), increased by 27 dB to approximate the power levels at the input to the transducer structure. The output power levels shown on the right side vertical axes of Figs. 3 and 7 are indicated in μW. These values correspond to the actual powers registered at the MTA input but increased by 2 dB to approximate the power levels at the output of the transducer structure. The peak signal levels for the forward traveling and reflected microwave pulse signals in with Figs. 5 and 6 are shown in mV. These values correspond to the input channel MTA signal voltages. The connection between a given MTA voltage V and power P follows the relation $P=\frac{1}{2}V^2/R$, where R is the 50Ω input impedance for the MTA channel. The V^2/R factor comes from Ohm's law. The factor of 1/2 is needed to connect the peak voltage readings for the 5.8 GHz signal to average microwave power. The voltage levels in Figs. 5 and 6 are shown on a logarithmic scale. Since the MSW power is proportional to the square of the dynamic magnetization response, the mV data correspond to the dynamic magnetization response amplitude rather than power. The decay in the mV signal level with either distance or time will yield the operational relaxation rate for the dynamic magnetization.

B. Nomenclature

A recent report by Hurben and Patton[14] contains a detailed review of the properties of magnetostatic backward volume waves in YIG films at microwave frequencies and under low power conditions. One of several key properties of these BVW excitations is their dispersion relation of frequency versus wave number. The dispersion relation for the BVW carrier frequency ω_k as a function of wave number k may be obtained from Ref. 14 according to

$$\cot(k_z^i S)=\frac{1}{2}\left[\frac{(\omega_k^2-\omega_H^2)-(\omega_B^2-\omega_k^2)}{\sqrt{(\omega_B^2-\omega_k^2)(\omega_k^2-\omega_H^2)}}\right] \tag{1}$$

and

$$k=\sqrt{\frac{\omega_B^2-\omega_k^2}{\omega_k^2-\omega_H^2}}\,k_z^i. \tag{2}$$

The parameter S in Eq. (1) denotes the film thickness. The ω_H and ω_B are frequency parameters defined by $\omega_H=\gamma H$ and $\omega_B=\gamma[(H+4\pi M_s)H]^{1/2}$, where M_s is the saturation

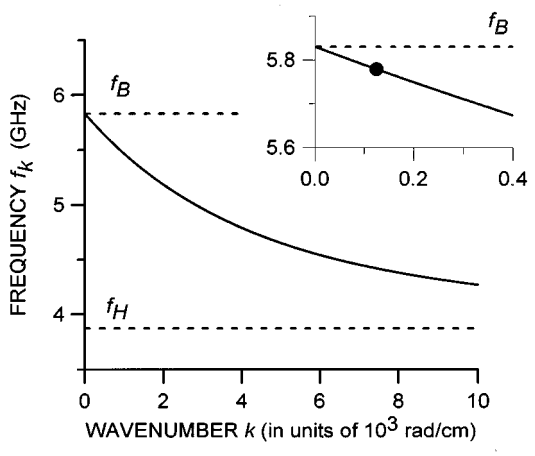

FIG. 2. Dispersion diagrams of magnetostatic backward volume wave frequency f_k vs wave number k. The horizontal dashed lines and the frequencies f_B and f_H denote band limits. The solid curves were calculated for a 5.1-μm-thick yttrium iron garnet film with an in-plane static field $H=1384$ Oe. The solid circle at $f_k=5.779$ GHz and $k=125$ rad/cm represents the operating point for the single-pulse experiments.

magnetization and γ denotes the absolute value of the gyromagnetic ratio for the electron magnetic moments in the material. The k_z^i parameter represents an effective wave-vector component for the mode profile across the film. For YIG at room temperature, the nominal value of $4\pi M_s$ is 1750 G. For free-electron moments corresponding to a Landé g factor, $g=2$, one has $\gamma=1.76\times10^7$ rad/Oe s for frequency in rad/s and $\gamma=2.8$ GHz/kOe in practical units. Note that the ferromagnetic resonance (FMR) frequency for in-plane magnetized isotropic magnetic films is at $\omega_{\rm FMR}=\omega_B$, even though the analyses for FMR and BVW excitations are for different limits. In the above formulas and for all analyses which follow, the Gaussian system of units is used. Frequencies in rad/s will be denoted by $\omega,\omega_k,\omega_H,\omega_B$, etc. These same frequencies, when specified in Hz or GHz, will be denoted by f, f_k, f_H, f_B, etc.

Figure 2 shows a dispersion curve for the lowest-order solution to Eqs. (1) and (2). The figure shows the magnetostatic backward volume mode frequency f_k, in GHz, as a function of wave number k, in rad/cm for the $4\pi M_s$ and γ values cited above, a film thickness $S=5.1$ μm and a field $H=1384$ Oe. This S value is the thickness for the YIG film used for the experiments considered below. The H value corresponds to the field used for the single-soliton pulse reflection experiments to be discussed in the next section. The inset in Fig. 2 shows an expanded view of the dispersion curve for the region near $k=0$. The curve in this expanded view is decorated by a solid circle at $f_k=5.779$ GHz and $k=125$ rad/cm. This is the frequency used for the single-pulse reflection experiments as well. The circle, therefore, corresponds to the operating point for these experiments. This operating point corresponds to a k_z^i value of 0.36 rad/cm or an across-the-film wavelength of 17 cm. The mode profile across the film is essentially uniform.

The dispersion curve starts at the top of the BVW band at $k=0$ and $f_k=f_B=5.83$ GHz. As the wave number k increases from zero, f_k decreases with an initial negative slope. The curve has positive curvature and gradually approaches a limiting frequency $f_k=f_H=3.87$ GHz in the limit $k=\infty$. The negative slope corresponds to a negative group velocity and is the origin of the term ''backward'' in the backward volume wave label. In the experiments, the input and output transducers define the propagation direction for the pulses and, hence, the direction of $\mathbf{v}_g$. Strictly speaking, backward volume waves will have the wave vector $\mathbf{k}$ directed opposite to the propagation direction rather than in the same direction as indicated in Fig. 1. The single-pulse measurements of the next section yielded $|v_g|$ values in the 2.57×10^6 cm/s to 2.77×10^6 cm/s range. The calculated value from $|v_g|=|\partial\omega_k/\partial k|$, Eqs. (1) and (2), and the parameters listed above is 2.52×10^6 cm/s. These values will be discussed in the next section.

Measurements of $|v_g|$ versus frequency yielded a value of 590 cm^2/rad s for the dispersion parameter $D=\partial^2\omega_k/\partial k^2$ at the operating point in Fig. 2. This compares reasonably well with the calculated value of 675 cm^2/rad s. These $|v_g|$ and D values are smaller than the corresponding values in Ref. 8 because the operating point k value is somewhat larger.

BVW wave-packet propagation is possible as long as one utilizes a carrier frequency located within the applicable band limits and sufficiently wide pulses to maintain a narrow spectral width which does not extend the frequency content of the pulse beyond the edges of the band. As already indicated, the group velocity of such pulses is determined by the frequency operating point within the band and the slope of the dispersion curve at that point. For a given propagation distance, as between the microstrip transducers in Fig. 1, the decay in pulse power due to damping will be smallest for the largest possible group velocity. This condition is accomplished by operating as close as possible to the f_B point in Fig. 2. As already indicated, the solid circle on the dispersion curve in Fig. 2 represents the 5.779-GHz operating point chosen for much of this work. The downshift of this operating point from the f_B band edge at 5.83 GHz, a shift of about 50 MHz, is needed because of the spectral width in frequency content caused by the finite pulse width. For a pulse width of 24 ns, the value used for many of the results given below, the spectral half width of the microwave pulse signal is about 20 MHz.

Turn now to the basic nonlinear properties for the BVW excitations. For a frequency operating point close to ω_B or f_B, the nonlinear effects which lead to soliton formation may be described to a good approximation in terms of an amplitude dependent ω_B band limit. Consider a right-handed x-y-z coordinate system for the in-plane magnetized film with the x direction perpendicular to the film, the y-direction in-plane, and the in-plane z direction along $\mathbf{k}$, $\mathbf{H}$, and $\mathbf{M}_s$. This configuration matches the setup for BVW wave-packet propagation in Fig. 1. To lowest order, one may describe the magnetization response for a propagating BVW signal as given below:

$$m_x(z,t)=i\sqrt{2}M_s\,\frac{\omega_H/\omega_B}{\sqrt{1+\omega_H^2/\omega_B^2}}\,u(z,t)e^{-i(kz-\omega_k t)}, \quad (3)$$

$$m_y(z,t)=\sqrt{2}M_s\,\frac{1}{\sqrt{1+\omega_H^2/\omega_B^2}}\,u(z,t)e^{-t(kz-\omega_k t)}, \quad (4)$$

$$M_z = M_s - \frac{|m_x(z,t)|^2 + |m_y(z,t)|^2}{2M_s} = M_s[1 - |u(z,t)|^2]. \quad (5)$$

The function $u(z,t)$ comprises a normalized complex envelope function for the BVW wave-packet dynamic magnetization amplitude. The precession is in the Larmor sense and corresponds to an elliptical polarization for the transverse x and y components of the dynamic magnetization according to

$$\frac{|m_x(z,t)|}{|m_y(z,t)|} = \frac{\omega_H}{\omega_B}. \quad (6)$$

This condition is strictly applicable only for an operating point close to the ω_B or f_B band edge.

The nonlinear response is obtained from the realization that the BVW upper band edge frequency limit $\omega_B = \gamma[(H + 4\pi M_s)H]^{1/2}$ applies only in the small signal limit for which $u(z,t)$ is small and M_z is very nearly equal to M_s. For large-amplitude excitations, one must write $\omega_B(M_z) = \gamma[(H + 4\pi M_z)H]^{1/2}$ and obtain, thereby, an amplitude-dependent band edge. One then may proceed to define a nonlinear response parameter N to describe the frequency shift in the operating point frequency ω_k with amplitude according to

$$N = \frac{\partial \omega_k}{\partial |u|^2}. \quad (7)$$

For an operating point frequency ω_k which is reasonably close to ω_B, N may be approximated by evaluating the rate of change in the band edge frequency ω_B with respect to $|u(z,t)|^2$.

From the above equations, along with the specified materials, field, and frequency parameters, one may readily obtain $N = -\omega_H \omega_M / 2\omega_B = -1.02 \times 10^{10}$ rad/s. One may also evaluate the rate of change in ω_k with $|u(z,t)|^2$ numerically, based on the dispersion equations given above and with ω_M replaced by $\omega_z = \gamma 4\pi M_z$. This procedure yields an N value of -1.0×10^{10} rad/s. This later value will be used for the numerical evaluations given below. It is important to note that the definitions of N vary in the literature, due mainly to different defined connections between the z component of the magnetization, M_z, and $|u|^2$. Equation (5) makes this connection in a simple way, but requires more complicated connections to obtain the transverse m_x and m_y components of the dynamic response in terms of u. An alternate approach, first introduced by Zvezdin and Popkov,[15] was used in Ref. 8. In any case, the final effect is the same, namely, an amplitude-dependent excitation frequency as defined through Eq. (7).

As discussed in the references cited in the Introduction, it is this nonlinear frequency shift which can, in certain situations, compensate for the wave-packet spreading caused by dispersion and produce solitons. One may note that the nonlinear coefficient N for BVW signals is *negative*, while the dispersion parameter D is *positive* for BVW excitations. BVW signals, therefore, satisfy the Lighthill criterion for soliton formation, $N \cdot D < 0$. Under conditions when the Lighthill criterion is satisfied, the working equation for theoretical soliton calculations is the nonlinear Schrödinger (NLS) equation. A practical form of this equation which may be directly applied to MME soliton experiments is given by

$$i\left(\frac{du}{dt} + \nu_g \frac{du}{dz}\right) + \frac{1}{2} D \frac{d^2u}{dz^2} - N|u|^2 u = -i\eta u. \quad (8)$$

All the parameters in Eq. (8) have been defined except the relaxation rate parameter η. This relaxation rate parameter described the losses or damping of the microwave magnetic response. In the linear response analysis, the transverse components of the dynamic magnetization decay according to $u(z,t) = u(0,0)e^{-\eta t} = u(0,0)e^{-(\eta/\nu_g)z}$. For solitons, however, one finds that the decay in u is at a somewhat faster rate.[16] In the experiments to be described shortly, it will be possible to measure these decay rates directly by measuring output signal power as a function of the transducer separation Z. The linear decay rate η will be found to be about 5×10^6 rad/s. This corresponds to a ferromagnetic resonance linewidth, which is approximately equal to $2\eta/\gamma$, of about 0.6 Oe. Such losses are typical of good-quality single-crystal YIG films.

The usual procedure for comparing theory to data for soliton experiments is to set up a boundary value problem with an initial $u(0,t)$ or $u(z,0)$ profile, use numerical methods to compute various $u(z,t)$ profiles for the propagating wave packets, and compare these calculated profiles with the measurements. Such comparisons may be found in Ref. 8. For the present purposes, however, only one relatively simple NLS equation solution result is needed, the analytical order one-soliton wave-packet amplitude solution from inverse scattering theory.[15] This amplitude, expressed in terms of the parameters already established, is given by

$$|u(z,t)| = u_0 e^{-2\eta t} \operatorname{sech}\left[(z - \nu_g t) u_0 e^{-2\eta t} \left|\frac{N}{D}\right|^{1/2}\right]. \quad (9)$$

Equation (9) is a solution to Eq. (8) in the limit of small damping. The amplitude u_0 refers to the initial peak value of $u(z,t)$ at some time $t = 0$ for the propagating wave-packet profile. Equation (9) demonstrates two little realized but critical properties of soliton pulses. First, note the $e^{-2\eta t}$ exponential decay term which multiplies the initial amplitude u_0. This term gives an amplitude decay rate of 2η, which is twice the usual rate for linear pulses. This more rapid decay for soliton pulses relative to linear pulses will provide one means of identification for soliton signals. The second important result comes from the appearance of the $u_0 e^{-2\eta t}$ amplitude factor inside as well as in front of the sech function. This leads to a soliton shape which becomes wider as the amplitude decays. This increase in width will provide another test of the soliton character of the pulse signals to be considered in the following sections. In order to put this inverse connection on a more quantitative basis, define the width Γ_t of the above sech function as the spread in time from one side of the pulse to the other for a reduction in amplitude $u_0/2$. In the limit of small damping and $\eta\Gamma_t \ll 1$, this theoretical soliton width at half the peak amplitude is given by

$$\Gamma_t = \frac{2\ln(2+\sqrt{3})}{u_0 \nu_g} \left| \frac{D}{N} \right|^{1/2}. \tag{10}$$

The comparison of the theoretical width with measured BVW pulse widths will be one test for soliton formation to be considered in Sec. III.

In considering MME soliton formation, four characteristic times for linear and nonlinear MME pulses are often of importance, the characteristic relaxation time T_r, a characteristic dispersion time T_d, a characteristic nonlinear response time T_n, and the propagation time from wave-packet launch to observation, T_p. These times are discussed in Refs. 7 and 8 and are not a major focus here. It will still be useful, however, to take note of their values.

The relaxation time T_r is simply the decay time of the dynamic magnetization response due to energy dissipation. If only relaxation is considered, the amplitude of the MME wave packet will simply decay according to $e^{-\eta t}$ with a characteristic $1/e$ decay time given by $T_r = 1/\eta$. Based on the η value cited above, 5×10^6 rad/s, T_r is 200 ns.

The dispersion time T_d may be defined as the time for a pulse of initial width T_0 and power amplitude $|u_0|^2$ to double its width due to dispersion. If one takes the spectral width in frequency for an initial MME pulse of width T_0 to be $2\pi/T_0$, one may obtain an approximate dispersion time

$$T_d = \frac{\nu_g^2 T_0^2}{2\pi |D|}. \tag{11}$$

For the parameters given above, one obtains $T_d(\text{ns}) = 1.92\,[T_0(\text{ns})]^2$. For $T_0 = 24$ ns, T_d is 1100 ns. Note that the T_d defined above is *smaller* than the dispersion time defined in Refs. 7 and 8 by a factor of 2π. This is due to the more realistic $2\pi/T_0$ value of the spectral width cited above. References 7 and 8 set this width at $1/T_0$.

The nonlinear response time may be defined as the time for the nonlinear frequency shift to yield a phase change of π between the original low power carrier signal and the shifted carrier signal at power amplitude $|u_0|^2$. This time is obtained as

$$T_n = \frac{\pi}{|N|\ |u_0|^2}. \tag{12}$$

For the N value given above, one obtains $T_n(\text{ns}) = 3071/[|u_0|\times10^2]^2$. Note that for T_n to fall in the 100–1000 ns range relevant to the current experiments, the $|u_0|\times10^2$ parameter must be on the order of 2–5. This corresponds to an initial $|\mathbf{m}|$ response on the order of 2–5 % of M_s.

The fourth characteristic time is the propagation time T_p for the low-amplitude wave-packet pulse in a particular experiment. In the context of the current experiments, this time is given simply by $T_p = Z/|\nu_g|$ for the pulses detected immediately after launched from the input transducer or $T_p = (2L - Z)/|\nu_g|$ for pulses after edge reflection. The distances for the experiments to be considered below range from about 5 to 15 mm with corresponding T_p values in the 200–600 ns range.

The interplay between these various characteristic times sets the conditions for both the linear pulse response at low power and the generation and observation of solitons at high power. In simple terms, the formation of solitons involves a compensation for the phase change between the wave-packet harmonic components caused by dispersion by the phase change caused by the nonlinear frequency shifts for these components. A rigorous treatment which includes the possibility of the generation of more than one soliton leads to[15]

$$T_0^2 |u_0|^2 > (n - 1/2)^2 \frac{\pi^2}{|\nu_g|^2} \left| \frac{D}{N} \right|, \tag{13}$$

where n is a positive integer soliton number which loosely corresponds to the number of solitons created. This result reflects the intuitive expectation that the *lower* the dispersion or the *higher* the nonlinear frequency response parameter N, the shorter the pulse width and/or the lower the power amplitude needed to produce solitons. Based on the parameters already indicated, Eq. (13) gives a critical $[T_0(|u_0|\times10^2)]^2$ product value for order one solitons of 200 ns^2. The soliton threshold for $T_0 = 24$ ns is at $|u_0|\times10^2 \approx 0.6$, or at an $|\mathbf{m}|$ value on the order of 1% of M_s.

There are additional constraints on $|u_0|^2$ which are related to the relaxation time T_r and the propagation time T_p. Consider relaxation first. The condition $T_n < T_d$ is already imbedded in Eq. (13). However, if the nonlinear response time T_n is *longer* than the relaxation time T_r, decay due to relaxation will dominate and the soliton generation will not be possible. Basically, the pulse decays before it has a chance to form a soliton. A second condition for solitons, therefore, is obtained from $T_n < T_r$. This amounts to a condition on the initial pulse power amplitude $|u_0|^2$ alone:

$$|u_0|^2 > |u_0|^2_{rn} = \frac{\pi}{|N|}\ \eta. \tag{14}$$

For the values of N and η already given, one obtains $|u_0|_m \times 10^2 = 3.9$. In other words, a dynamic response with $|\mathbf{m}|$ on the order of 4% of M_s is needed to form a soliton in the presence of relaxation.

Now consider the propagation time constraint. In order to observe solitons which have been completely formed, the propagation time T_p should be *longer* than the nonlinear response time T_n. This amounts to a *second condition* on the initial pulse power amplitude $|u_0|^2$,

$$|u_0|^2 > |u_0|^2_{pn} = \frac{\pi}{|N|} \frac{|\nu_g|}{1\ \text{cm}}. \tag{15}$$

A distance of 1 cm is inserted in Eq. (15) to represent a typical propagation distance. For the parameter values already given, one obtains $|u_0|_{pn} \times 10^2 = 2.9$. Here too, the level of $|\mathbf{m}|$ required for solitons is on the order of a few percent of M_s.

None of the above limits represent hard conditions on either the creation or the observation of soliton behavior. Note first that the various characteristic times are defined somewhat arbitrarily, in terms of a $1/e$ decay for T_r, a doubling in pulse width for T_d, and a phase change of π for T_n. Other definitions could have been used as well. The levels obtained above, therefore, represent more a rule of thumb than a definite threshold for n solitons. The damping and propagation time constraints, moreover, simply mean that whatever behavior is observed may correspond to additional damping effects or incomplete soliton formation. The key

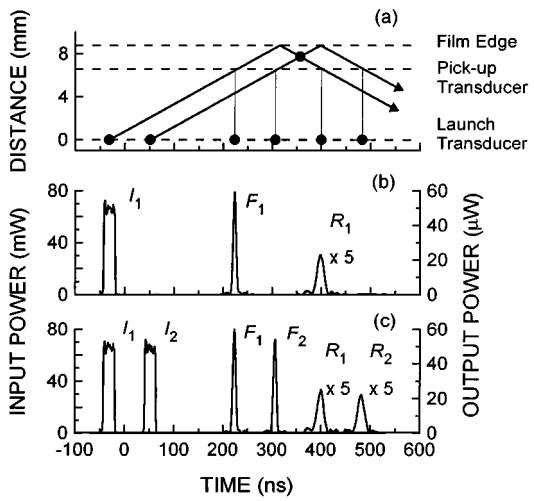

FIG. 3. Representative trajectories and pulse profiles for the single- and double-pulse experiments in the backward volume wave configuration for the 5.1-μm-thick yttrium iron garnet film strip, a static magnetic field of 1384 Oe, and a carrier frequency of 5.779 GHz. The pulse width was 24 ns. (a) Schematic trajectories of position relative to the input transducer vs time for the two-pulse experiment, with pulse reflection at the film edge position, detection at the pickup transducer position, and pulse collision at the position of the solid circle. (b) Input and output soliton pulse signals vs time for the single-pulse experiment. (c) Input and output soliton pulse signals versus time for the two-pulse experiment. The nominal position of the output transducer relative to the input transducer was 6.6 mm. The nominal spacing between the output transducer and the reflecting film edge was 2.2 mm.

points are that (1) a dynamic magnetization $|\mathbf{m}|$ response on the order 1% of M_s is needed to produce solitons and (2) the time scales for soliton formation are in the 100–1000 ns range.

One further result which will be needed for the analysis of the data to follow concerns the connection between the power flux P_{MSW} for the propagating BVW signal and the dynamic magnetization response $|\mathbf{m}|$ for the mode. A simple connection between these two parameters can be obtained from the basic response equations defined above and Maxwell's equations, under the assumption of a uniform dynamic response across the width and thickness of the film.[17] The result, expressed in Gaussian units, may be written as

$$|\mathbf{m}|^2=\frac{\omega_M}{\omega_H}\left(1+\frac{\omega_H^2}{\omega^2}\right)\frac{P_{\mathrm{MSW}}}{16SW|\nu_g|}. \tag{16}$$

This connection will prove useful for the analysis of the pulse reflection data in the next section.

III. PROPAGATION AND REFLECTION OF BVW MME SOLITONS

Some typical pulse measurement results from the edge reflection experiment are shown in Fig. 3. The particular results shown are for nominal values for Z and L of 6.6 and 8.8 mm, respectively, a pulse width of 24 ns as already indicated, and power levels which correspond to soliton propagation over the range of the data shown. The input power of 70 mW was above the minimum power required to produce solitons but below the power at which multisoliton profiles occur. More detailed results on soliton propagation and reflection will be presented shortly. The focus here is on the pulse timing and sequencing when edge reflection is involved. Figure 3 shows results for two different experiments, one with a single input pulse and one for two input pulses. Figure 3(a) shows trajectories for the two pulses in a distance versus time format. The solid circles and vertical lines denote the launch times and the detection times at the pickup transducer. Figure 3(b) shows the input and output pulse signals as a function of time for a single-pulse experiment and Fig. 3(c) shows the corresponding signals for a two-pulse experiment. The zero time reference is arbitrary. The input and output power scales for Fig. 3 were discussed in Sec. II. They are included simply to indicate the range of input and output power levels for the experiment. The accurate determination of relative changes in output peak powers with transducer position will be critical to the measurements to be presented shortly, however. The focus of this section is on the single pulse experiment results of the type shown in Fig. 3(b). Results for the two-pulse collision experiment will be considered in Sec. IV.

As evident from Figs. 3(a) and 3(b), the single-pulse experiment involves the launch of a rectangular pulse I_1, the forward propagation of that pulse along the film and past the point of the pickup transducer to produce signal F_1, and then reflection of the pulse from the end of the film to produce a second signal R_1 as the pulse passes the pickup transducer traveling in the reverse direction. The basic measurements to be presented in this section concern (a) the positions in time and (b) the amplitudes for the F_1 and the R_1 pulses as a function of pickup transducer position. Such data, as will be evident shortly, can provide three important pieces of information: (1) the position of the reflecting film edge, (2) ranges of incident power which produce linear and soliton signals, and (3) a quantitative power transfer factor for the fraction of the soliton pulse signal which is actually transferred to the pickup transducer. One important feature of the profile data in Fig. 3(b) is evident from the relative widths of the F_1 and R_1 pulses. The reflected R_1 pulse is clearly wider than the forward traveling F_1 pulse. This widening occurs even though the two signals represent the same soliton. It is due to the connection between the soliton peak amplitude and the soliton width embodied in Eq. (9). As the soliton decays in amplitude, the width increases. The experimental connection between soliton amplitude and width will be established at the end of this section.

Figure 4 shows the results of measurements of pulse timing as a function of the pickup transducer position relative to the input transducer, for two different input peak power values. The position of the reflecting film edge, relative to the launch transducer, was held fixed at a nominal value around 10 mm. The input peak power was 3.7 mW for the low power results in Fig. 4(a) and 145 mW for the high power results in Fig. 4(b). As will be made evident shortly from corresponding data on pulse power, the 3.7-mW input power produces linear pulses and the 145-mW power produces soliton pulses. The horizontal Z scale in Fig. 4 indicated the nominal separation between the input transducer and the

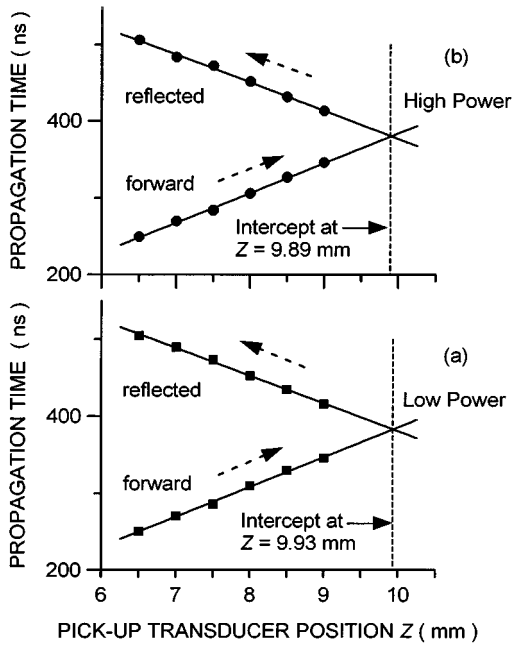

FIG. 4. Representative data on pulse propagation time vs pickup transducer position for the forward traveling and reflected pulse propagation experiment under low- and high-power conditions and with other operating parameters the same as for Fig. 3. The low-power data in (a) are for an input power of 3.7 mW and the high-power data in (b) are for an input power of 145 mW. The solid lines show the results of linear best fits to the data. The dashed lines indicate crossover positions for the forward traveling and reflected pulses for each graph.

pickup transducer in mm, as measured directly from the vernier scale on the translation stage. The vertical time scale represents the time for the peak in the forward traveling or reflected pulse at the pickup transducer measured relative to the time for the leading edge of the input pulse at the half amplitude point in voltage.

The Z values and time points shown in Fig. 4 yield pulse velocity determinations to be presented shortly. If these average velocity values and the timing data are extrapolated backwards to determine transducer spacings, one obtains values which are smaller than the indicated Z values by about 0.1 ± 0.05 mm. These differences are within experimental error for the distance determinations. Note also that the transducer widths are 50 μm or 0.05 mm. All transducer separation determinations must be uncertain to this dimension in any case. The important effects come from the change in the pulse position in time as the pickup transducer is moved relative to the launch transducer.

The solid lines in Fig. 4 indicate linear least-squares fits to the time versus position data for the four sequences of timing measurements shown. The vertical dashed lines in the two graphs designate the crossover points for the linear fits to the forward and reflected data sequences in each case. The numerical values of these intercepts are also indicated.

The two sets of data in Fig. 4 show clearly the propagation characteristics for the forward traveling and reflected pulse signals at low and high powers. The lower set of points for each graph represent the increase in the pickup time for the forward traveling pulse as the pickup transducer is moved away from the launch transducer. The slope of the response in each case represents the group velocity for the forward traveling pulse. The fitted low and high power forward traveling pulse group velocities are 2.58×10^6 and 2.57×10^6 cm/s, respectively. The standard deviation from the mean for these velocity determinations was 0.92 and 0.85%, respectively.

The higher set of points for each graph represents the decrease in the pickup time for the reflected pulse as the pickup transducer is moved closer and closer to the film edge. The slope of the response in each case represents the negative of the group velocity for the reflected pulse. The fitted low and high power pulse group velocities for the reflected pulses are 2.77×10^6 and 2.71×10^6 cm/s. The standard deviation from the mean for these velocity determinations was 0.85 and 1.18% for these two determinations, respectively.

The vertical dashed line intercept points for the two graphs in Fig. 4 will turn out to be important parameters for the results to follow. These intercepts, from the low- and high-power fits, respectively, are 9.93 ± 0.09 and 9.89 ± 0.11 mm, where the errors indicate standard deviations from the mean. The average intercept is equal to 9.91 ± 0.1 mm. This intercept corresponds to the extrapolated Z value for the pickup transducer at the film edge.

It is noteworthy that the fits in Fig. 4 give rather accurate but different group-velocity values for the forward traveling and reflected signals. The 1% random errors in the fits are significantly smaller than the 6% differences in these two velocities. The origin of these differences has not been investigated. They may be related to small misalignments between the static field and the YIG strip or anisotropy effects for the film. The 6% difference in velocities will have little impact on the results considered below. Where needed below for purposes of calculation, an average $|\nu_g|$ value of 2.66×10^6 cm/s will be used.

Figure 5 shows measurement results on the decay in pulse peak amplitude for the same pulse experiments used for the data shown in Fig. 4. The graphs display the peak detected voltage at the MTA for the pickup transducer. The two graphs are for the same low- and high-power conditions as in Fig. 4, with the peak input power set at 3.7 mW for Fig. 5(a) and at 145 mW for Fig. 5(b). The vertical axes in Fig. 5 show peak output pulse voltages obtained from the pickup transducer as recorded by the MTA. The horizontal axes in Fig. 5 are the same as in Fig. 4. For the discussion to follow, it will be important to keep in mind that each voltage-position data point in Fig. 5 has a corresponding voltage-time data point. A full analysis of the results will require consideration of both position and time points.

As discussed above, the vertical scales gives peak signal levels in millivolts as detected at the MTA. The 100 mV voltage level corresponds to a detected MTA peak power of 100 μW. For a cable attenuation of 2 dB, one then has about 160 μW at the output of the transducer structure. The actual transducer pickup powers are not needed for the analysis of the data in Fig. 5. They will be important for the determination of actual soliton peak powers, as will be considered shortly.

Note that the vertical scales for both graphs are logarithmic. The linear character for the individual plots or plot seg-

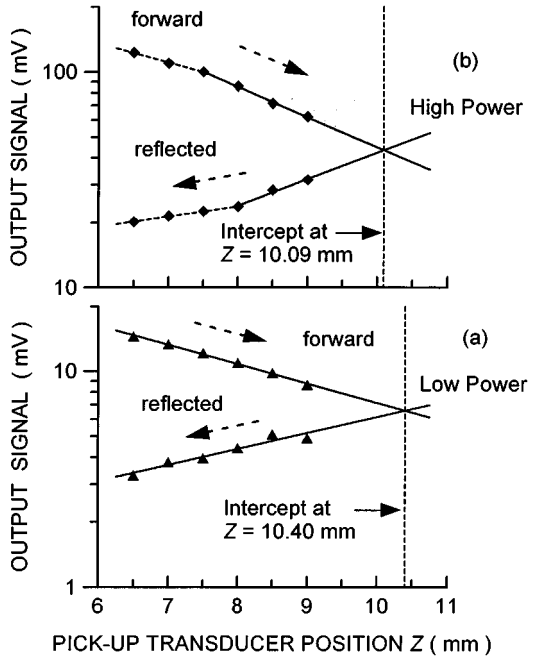

FIG. 5. Representative data on and fits to data on output pulse peak detected voltage vs pickup transducer position for the forward traveling and reflected pulse propagation experiment under low- and high-power conditions and with other operating parameters the same as for Figs. 3 and 4. The low-power data in (a) are for an input power of 3.7 mW and the high-power data in (b) are for an input power of 145 mW. The solid lines show the results of linear best fits to the segments of data tracked by the lines. The dashed lines indicate apparent crossover positions for the forward traveling and reflected pulses for each graph.

ments is indicative of a constant decay rate for those data. The relaxation rate η introduced in Sec. II is equal to the slope of the semilogarithmic response of voltage as a function of time for a given curve or curve segment multiplied by ln(10). The various straight lines in Fig. 5 indicate linear fits to various parts of the data.

The vertical dashed lines indicate fitted crossover points in position Z for the linear fits to the forward traveling and reflected pulse data at large Z values. These crossover points further indicate an *apparent* film edge position which is based solely on the pulse amplitude versus distance data. These apparent edge positions turn out to be somewhat larger than the film edge position obtained from the fits shown in Fig. 4. These different film edge positions have important implications which will be considered in detail at the end of this section.

The two-signal level vs position graphs in Fig. 5 have the same general character as the signal level vs time graphs in Fig. 4. For a given graph, the data points at the higher voltage levels, which decrease in voltage as the Z position is increased, represent the forward traveling pulses. The data point at the lower voltage levels, which increases as the Z position is increased, represents the reflected pulses. It is important to note that low power data in Fig. 5(a) show a nearly linear response on the semilogarithmic scale of the display, with about the same decay rates for the forward traveling and the reflected pulses. For the high power data, however, both the forward traveling pulse decay and the reflected pulse decay results appear to separate into two regions, one with a lower decay rate at small Z values and one with a higher decay rate at large Z values. As will be discussed shortly, the higher decay rate region is one indication of soliton propagation.

Consider first the low-power results in Fig. 5(a). The data show two important results, one concerning decay and one concerning crossover. Consider decay first. The linear decay in voltage versus propagation distance on the semilogarithmic scale shown is indicative of the constant low-power relaxation rate for the MME peak signal dynamic magnetization amplitude. Note that the actual power would correspond to the square of the voltage so that the voltage itself corresponds to the dynamic magnetization amplitude. The fitted slope for $\ln V$ versus Z corresponds to a spatial decay rate $\beta = \eta/|\nu_g|$. The fitted slope for $\ln V$ versus time corresponds to the actual relaxation rate parameter η. Low-power decay rates were obtained from the straight-line least-squares fits to the amplitude versus time. The fitted relaxation rates for the forward traveling and reflected pulses at low power were 5.3×10^6 and 4.7×10^6 rad/s, respectively. These rates convert to equivalent ferromagnetic resonance half power linewidths of 0.60 and 0.53 Oe, respectively. Such linewidths are quite reasonable for high-quality single-crystal YIG films of the sort used here. The deviation from the mean for the above η values amounted to about $\pm2\%$ for the forward traveling pulse data and $\pm5\%$ for the reflected pulse data, which is marginally consistent with the 12% difference in η values. As with the group velocity determinations discussed above, these small but possibly significant differences in the η values for the forward traveling and reflected pulses do not affect the results presented here and have not been explored further. For purposes of analysis and where needed, an average low-power relaxation rate parameter η was taken to be equal to 5×10^6 rad/s.

Now consider the crossover result for the data in Fig. 5(a). The vertical dashed line at $Z=10.4$ mm shows the intersection of the linear best-fit lines for the forward traveling and reflected pulse data. The actual fitted intersection point was at $Z=10.40\pm0.28$ mm, where the error gives the deviation from the mean. Naively, one might expect this intersection to be at the same Z value as for the pulse timing data in Fig. 4(a). That intersection was at $Z=9.93\pm0.09$ mm. In spite of the large errors in both intersection values, it is clear that the intersection point is at a larger Z value for the fitted decay data than for the timing data. There is a simple explanation for this discrepancy. As the forward traveling pulse travels across the pickup transducer and produces an output signal, the power which is picked off for detection reduces the power of the still propagating pulse. Hence, the voltages corresponding to the actual forward traveling pulse are somewhat smaller than the data points would indicate. In order to obtain an intersection point which is representative of the film edge reflection, one would need to shift all the data points for the forward traveling pulse down in voltage by some fraction to reflect the fraction of power picked off by the antenna.

This effect is more than an interesting aside. As will be discussed shortly, one has the same effect at high power. The mismatch in intersection points for the actual data in both

cases will make it possible to determine the pickup factor for the antenna. Since one can measure the detected power absolutely, this pickup factor makes it possible to determine the absolute peak power for the pulse incident on the antenna. The determination of this absolute power, moreover, makes it possible to correlate pulse peak power with pulse width and compare the empirical correlations with soliton predictions.

Turn now to the high-power results in Fig. 5(b). As with Fig. 5(a), two important effects are evident from the data, one concerning decay rates and one concerning crossover. Consider the decay rate effect first. It is clear that the decay rates for the data in Fig. 5(b) are segmented. The forward traveling pulse starts off with a low decay rate and changes to a higher decay rate for Z positions above about 7.5 mm. Further, the reflected pulse starts out, for $Z \approx 10$ mm or so, with about the same higher decay rate just before reflection, but then returns to a lower decay rate for Z positions below about 8 mm.

The steps in Z which were used for the measurements were too large to pinpoint the transition regions more accurately. Nevertheless, the effect is clear. After launch and for some time following launch, the propagating high power pulse goes through a formation process. The position of the transition at $Z \approx 7.5$ mm, combined with the previously measured propagation times, indicates that this formation time is on the order of 300 ns or so. The fitted relaxation rate in this region was 5.9×10^6 rad/s, with a standard deviation from the mean of 2%. This rate is about 10% higher than the corresponding low-power incident pulse decay rate.

For $Z > 7.5$ mm, the fitted relaxation rate increases to 7.8×10^6 rad/s, with a standard deviation from the mean of 1%. This rate is a factor of 1.5 higher than the corresponding low-power incident pulse decay rate. In previous work, this increase in the decay rate has been associated with the propagation of solitons.[16] It is reasonable, therefore, to interpret the present incident pulse high-power data in terms of (i) a formation region over which the interplay between nonlinear response and dispersion works to produce the MME soliton, followed by (ii) a region over which the more or less formed soliton propagates forward in the film. A soliton formation time of 300 ns or so is reasonable from the considerations given in Sec. II. Recall that the dispersion time parameter T_d was estimated as about 1000 ns. For a nonlinear response time T_n in the 100–1000 ns range, one requires an input dynamic magnetization amplitude $|\mathbf{m}|$ on the order of 2–5% of M_s. Further, the single-soliton threshold condition of Eq. (13) indicates a minimum input dynamic magnetization amplitude $|\mathbf{m}|$ of about 1%. Recall that none of these considerations represent hard conditions for MME solitons. The range of numbers, nevertheless, is consistent with the formation-to-soliton effect identified from Fig. 5(b).

The reflected pulse data in Fig. 5(b) support the soliton hypothesis as well. Immediately after reflection, the decay rate is approximately the same as immediately before reflection, but is then reduced for Z values below about 8 mm. This is because, initially after reflection, the pulse still has sufficient amplitude to maintain its soliton character. As it decays, however, the amplitude becomes insufficient to support a soliton pulse and the propagation characteristics revert to those expected at low power. For the reflected pulse signal and soliton region Z values from 8 to 9 mm, the fitted relaxation rate is 7.5×10^6 rad/s, with a standard deviation from the mean of 3%. This rate is a factor of 1.6 higher than the corresponding low-power reflected pulse relaxation rate. As with the forward traveling pulse result, this higher relaxation rate is one indication of soliton propagation. Once the pulse moves to Z values below 8 mm, the fitted relaxation rate drops to 3.0×10^6 rad/s, with a standard deviation from the mean of 3%. This rate is a factor of 0.6 smaller than the corresponding low-power reflected pulse relaxation rate. The reasons for this apparently anomalous drop are not known. Dispersion may be a factor here, in spite of the relatively long initial pulse width.

Note that the peak signal voltage at which the decay rate changes from the soliton value to the lower value is about 25 mV, compared to the 100 mV value for soliton formation from the forward traveling pulse data, for an amplitude ratio of four. It is not possible to obtain a ratio of amplitudes for the soliton at formation and at changeover back to a dispersive pulse from the simple working equations of Sec. II. One may, however, use the fact that all the high-power pulse profiles had a single-peak character similar to the profiles in Fig. 3 to argue that the pulses correspond at most to $n=1$ solitons. From Eq. (13), one must have a factor of 3 increase in $|u_0|$ to go from $n=1$ to 2 solitons. These ratios are certainly in the same range. The factor of 4 drop in amplitude from soliton formation to changeover is certainly reasonable.

The basic crossover effect for the high-power data is the same as discussed above in connection with the low-power data. The high-power intersection point for the linear fits to the forward traveling and reflected soliton pulse data is at $Z = 10.09 \pm 0.24$ mm. Recall the intersection point of 9.89 ± 0.11 mm obtained from the timing data for the high power pulses. In spite of the large errors, these data indicate the same power pickup effect discussed above. This section on the propagation and reflection of soliton pulses is concluded with an analysis of this pickup effect and its implications for MME soliton measurements.

The timing data from Fig. 4 and the voltage decay data from Fig. 5 have been combined to yield the low- and high-power semilogarithmic graphs of MTA voltage versus time shown in Fig. 6. The format is the same as for Figs. 4 and 5. As before, Fig. 6(a) is for the low-power data and Fig. 6(b) is for the high-power data. The top left set of points in Fig. 6(a) corresponds to the six data points for the forward traveling pulses and the dashed line through those points represents the linear best fit to the data. The top left set of points in Fig. 6(b) correspond to the four data points for the forward traveling soliton pulses and the dashed line through those points represents the linear best fit to these data. Note that the slope of the linear fit for the soliton data is steeper than for the low-power pulse data. These slopes give the relaxation rates in these regimes. As indicated above, the soliton regime high-power relaxation rate is a factor of 1.5–1.6 greater than that for the low-power pulses.

The lower set of points in Fig. 6(a) corresponds to the six data points for the reflected pulses at low power. The dashed line through those points represent the best fit which could be obtained by shifting the linear best fit to the forward pulse data down by a constant factor. The fit reduction factor needed to produce this line was 0.872, as indicated on the

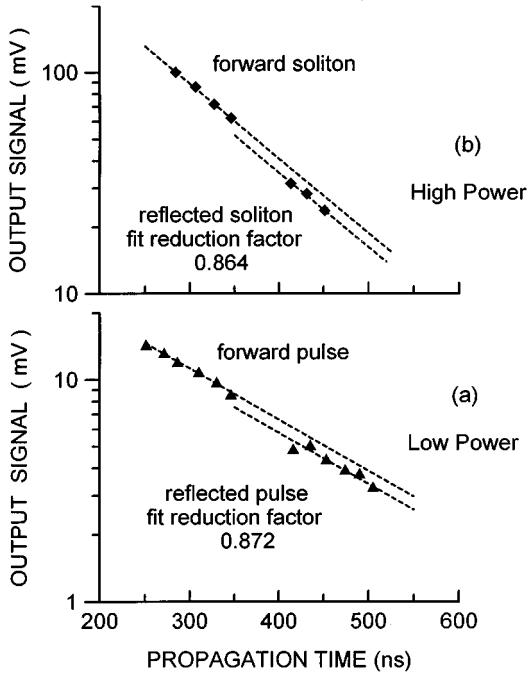

FIG. 6. Data and fits to data on output pulse peak detected voltage vs propagation time for the forward traveling and reflected pulse propagation experiment under low- and high-power conditions and with other operating parameters the same as for Figs. 3–5. The low-power data in (a) are for an input power of 3.7 mW and the high-power data in (b) are for an input power of 145 mW. The dashed lines through the forward pulse and forward soliton data show the results of linear best fits to the data. The dashed lines through the reflected pulse and reflected soliton data show these same lines shifted down by the indicated fit reduction factor.

graph. The standard deviation of the six data points from the dashed line fit amounted to an error of about 35%. The lower set of data points in Fig. 6(b) corresponds to the three data points for the reflected soliton pulses. The dashed lines through those points represent the best fit which could be obtained by shifting the linear best fit for the forward pulse soliton data down by a constant factor. The fit reduction factor needed to produce this line was 0.864. The standard deviation of the three data points from the dashed line amounted to an error of about 10%.

Based on the remarks already provided concerning the mismatch in crossover points obtained from the pulse timing data and the voltage decay data, the downward shifts in signal voltages from the forward pulses to the reflected pulses are readily explained in terms of power pick off at the transducer. It is noteworthy that the fit reduction factors at low power and at high power are essentially the same, in spite of the very different pulse decay characteristics. Note also that these factors refer to the MSW signal amplitude and not power. The corresponding transducer power pickup factor is given by $[1-(0.87)^2]$, or approximately 0.25. In other words, the pickup transducer picks off about 25% of the power from the MSW pulse as it propagates across the transducer. Such a pickup is clearly significant.

This pickup effect was not anticipated, and the error is too large to place a value on this pickup factor with great precision. Furthermore, one should also consider any loss of signal due to the edge reflection before ascribing all of these losses to transducer pickup. Tsankov and co-workers found that this effect is small for forward volume MSW signals.[7] This possible loss contribution will not be taken into account here. In order to place these effects on a quantitative footing, however, precision decay measurements for two pickup transducers and variable distances will be needed.

In spite of the lack of accuracy, it will prove instructive to use this pickup power factor to estimate the actual absolute peak power for a given soliton pulse incident on the pickup transducer and use this power to estimate the soliton amplitude $|u_t|$. It will then be possible to examine the relation between the various $|u_t|$ values and measured pulse widths. Equation (10) provides a simple relation between $|u_t|$ and the order one soliton half width Γ_t under the assumption of small damping. A comparison of this simple theoretical prediction with the present data will prove instructive. Because of the aforementioned error problems, no extensive interpretation can be made. The results below are intended only to demonstrate the possible correlations with simple one soliton theory and to point out possible problems.

The working equations for the above procedure are Eqs. (10) and (16), along with the implicit connection between $|\mathbf{m}|^2$ and $|u|^2$ from Eq. (5), $|u|^2=\frac{1}{2}|\mathbf{m}|^2/M_s^2$. The peak signal voltage V in volts at the MTA for a given data point in Figs. 4 or 5 is first converted into a value for the MSW power incident on the pickup transducer, P_{MSW}, according to the relation $P_{\mathrm{MSW}}=[V^2/100][10^{+2/10}][2][4][10^7]$. The divisor of 100 is from the P-V relation for the MTA system given in Sec. II A, the $[10^{+2/10}]$ factor accounts for the 2 dB attenuation in the line from the pickup transducer to the MTA, the [2] accounts for the bidirectional pickup of the strip line, the [4] derives from the 0.25 MSW power pickup factor at the antenna, and $[10^7]$ converts power from J to ergs. One then uses Eq. (16) to obtain $|\mathbf{m}|$ and Eq. (5) to obtain the dynamic magnetization wave-packet reduced peak amplitude $|u_t|$. One measures the experimental half width for the corresponding pulse voltage signals to obtain the pulse width Γ_t. Finally, the theoretical connection between $|u_t|$ and Γ_t is obtained from Eq. (10).

Results from the above procedure are shown in Fig. 7, where pulse width is shown as a function of the peak amplitude. Amplitude is given in percent of the saturation magnetization M_s. The four different symbols designate the four different pulse regions identified in connection with Fig. 5. The circles are for the forward traveling pulse in the soliton formation region, the squares are for the forward traveling pulse in the soliton regime, the diamonds are for the reflected soliton signal, and the triangles are for the reflected pulse after decay back to the linear range. The solid line gives the result from Eq. (10).

Consider first the data points for the highest peak amplitude values in the 1.5–2.5% range. The experimental results in Fig. 7 show that these high-power pulses, which correspond to the soliton formation and soliton propagation forward traveling regimes, have widths which are in reasonable agreement with the predictions for simple order one solitons with no damping. If there is appreciable loss associated with edge reflection, the data points will be shifted further to the left and away from the theory. It is important to note that no adjustable parameters have been invoked for the results

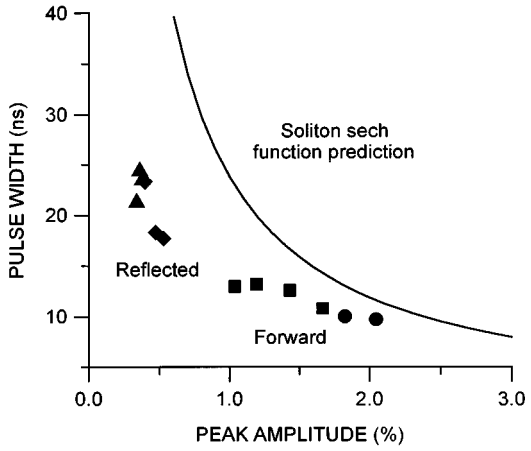

FIG. 7. Pulse width as a function of peak amplitude, according to the definitions given in the text. The solid points are from the high-power signals shown in Figs. 4–6, and discussed in the text. The circles are for the forward traveling pulses in the soliton formation regime, the squares are for the forward traveling soliton pulses, the diamonds are for the reflected soliton signals, and the triangles are for the follow-on residual linear pulses in the reflected range. The solid curve gives the theoretical prediction for simple order 1 soliton sech pulses.

shown. The data points derive purely from the measurements and the Eq. (6) connection between the MSW power and the dynamic response. The theoretical curve derives from Eq. (10), with known parameters. From these results, it appears that as the soliton first forms, its properties are fairly close to those expected from a simple undamped order 1 soliton sech response.

Move now to lower powers and amplitudes, and follow the data points for the reflected soliton and residual regimes. Here, it is seen that the pulse widths do increase somewhat as the amplitude decreases, but the rate of change is much smaller than expected for the simple sech-type soliton. This less rapid increase in pulse width, relative to the simple theory, may be due to some combination of several factors. First, the theoretical result is valid only in the limit of small damping. The damping here is not small. Second, close inspection of the actual pulse shapes reveals profiles which, in general, are not at all like simple sech functions. The pulse signals are asymmetric and are decorated by additional side lobes and, in some cases, background level voltages which make it difficult to determine simple width parameters.

It is also important to take note of various sources of error for the results in Fig. 7. Consider experimental errors first. If one assumes an error of ± 0.05 for the MSW power pickup coefficient and an error of ± 0.5 dB for the 2-dB attenuation factor, the error in the peak amplitude values on the horizontal axis is about $\pm 15\%$. The measurement error in the pulse widths was below ± 1 ns. However, the actual pulse shapes were not particularly symmetric and baselines were not well defined. The practical error in the pulse width determinations was closer to ± 5 ns. Recall also that the antenna power pickup factor of 0.25 was obtained by ignoring any possible loss due to the edge reflection. A 1-dB edge reflection loss charges our 0.25 factor to 0.31 and reduces the peak amplitude values shown in Fig. 7 by approximately 10%. An additional source of error may lie in Eq. (10). The actual propagating BVW mode in the narrow YIG strip may be more complicated than that used in the model calculation.

In summary for this section, the formation, propagation, and reflection properties of MME BVW soliton pulses has been examined in detail. Group velocities which are essentially unchanged from that at low power. One obtains a clear signature, both for the formation of the MME solitons after a time from launch of several hundred ns and for the changeover back to low power propagation characteristics after a drop in amplitude by about a factor of 4. The reflection of pulses from the end of the YIG film allows for the experimental determination of an antenna power pickup factor. This factor, in turn, allows one to estimate the absolute soliton amplitude and calculate soliton widths for comparison with measurements. While the error in these determinations is not small, the results are reasonable. Future precision measurements of these properties should make it possible to characterize quantitatively the amplitudes, widths, and overall response profiles for MME solitons.

IV. INTERACTION AND COLLISION OF BVW MME SOLITONS

The collision experiment was carried out by launching single pulses and two pulses in sequence, observing a first series of pickup signals as these pulses pass by the output transducer, and then observing a second series of signals after the pulses reflect off the film edge and travel back by the output transducer in the opposite direction. Typical results for pulse power levels in the soliton regime established above were shown in Fig. 3. The Sec. III discussion of Fig. 3 was intended only to establish the basic nature of the propagation and reflection experiment. Here, the focus is on the implications of these data and similar results at high power levels which illustrate the effects of collision for these nonlinear MME pulses.

Recall that the input power level was the same for the single- and double-pulse traces shown in Fig. 3. Recall, further, that this power level was chosen (1) to produce pulses which would form solitons before the forward detection points for the F_1 and F_2 pulses and (2) be sufficient to allow the propagating pulses to retain their soliton character long enough for reflection and a second detection of the R_1 and R_2 pulses. Through this arrangement, one produces the collision situation depicted in the top diagram of Fig. 3. This diagram illustrates the trajectories of the two pulses in the experiment. When two pulses are launched, the MME wave packets collide prior to the detection of the reflected R_1 and R_2 pulses. The MME pulse profiles shown in the bottom and middle graphs demonstrate that the collision has little or no effect on the individual pulse shapes.

The middle graph in Fig. 3 shows the shapes for the F_1 and R_1 pulses when there is no collision. The soliton propagation is accompanied by the same rapid decay in amplitude discussed above and analyzed in detail in connection with Figs. 5 and 6. There is no change in shape from the F_1 profile to the R_1 profile. The widening of the R_1 pulse relative to the F_1 pulse is a consequence of the soliton pulse shape indicated in Eq. (9), which demonstrates the connection between pulse width and amplitude. In the limit of small

damping, one would expect that the product of the pulse width and amplitude would be constant. A detailed examination of the pulses in Fig. 3 indicates that the amplitude width product is reduced by a factor of 0.6 from F_1 to R_1. This difference is probably a consequence of the large decay rates which are on the order of the propagation times. Apart from these details, the point to be emphasized is that the soliton properties for the pulse have been established. One needs to keep the shapes of these pulses in mind as the effect of collision is considered.

The double pulse results in the bottom graph of Fig. 3 demonstrate the effect of such collision. The delay time between the input pulses of 85 ns or so allows for collision to occur roughly midway between the pickup transducer and the reflecting film edge. The collision occurs between the reflected initial pulse and the still forward traveling second pulse. As the bottom R_1 and R_2 profiles indicate, the collision has virtually no effect on either pulse. The initial F_1 and F_2 pulses are identical and the reflected R_1 and R_2 pulses are also identical. This shows that the two single-soliton pulses pass through each other intact and retain their original character at pickup. To the accuracy of the group velocity measurements, the head-on collision between the two solitons also does not change their velocities.

The collision survival property was found to persist for power levels as high as 4 dB above the single-soliton regime of Fig. 8(a). With a further increase in the input power level, however, several new and striking effects have been found. This report on formation, propagation, reflection, and collision of MME solitons will be concluded with a brief report on these new effects.

As is well known, the pulse shapes for the individual forward traveling soliton pulses begin to show a double-peak character for powers well above the single-soliton threshold. This additional peak indicates the formation of an order 2 soliton. The effects of higher powers on soliton profiles and the quantitative measurement of higher-order soliton properties have been discussed in detail in Refs. 7, 8, 18, and 19. Due to limitations in power and constraints due to the large decay rates for the soliton signals, it has not been possible to extend the above collision considerations into the multisoliton regime. In order to do so, one would need to apply the same considerations discussed in Sec. III to ensure the propagation of an order 2 soliton, for example, over the entire range of propagation and reflection times. This has not been possible. It has been possible to go to powers somewhat higher than those discussed above and observe additional effects.

Figure 8 shows representative data for the collision effects which have been found for input power levels a factor of 3 or so above the input power level used for the data in Fig. 3. Figures 8(a) and 8(b) are identical to the corresponding graphs in Fig. 3. Figures 8(c) and 8(d) follow the same format but show the effects of the higher input power on the pulse profiles. The input power of 210 mW was a factor of 3 larger for Figs. 8(c) and 8(d) than for Figs. 8(a) and 8(b). It is also 45% larger than the high-power level for Figs. 4–6.

Consider first the graph for the single-pulse experiment in Fig. 8(c). Here, the F_1 pulse no longer has the single-peak character associated with order 1 solitons. The data show the beginnings of the formation of a second peak after the first

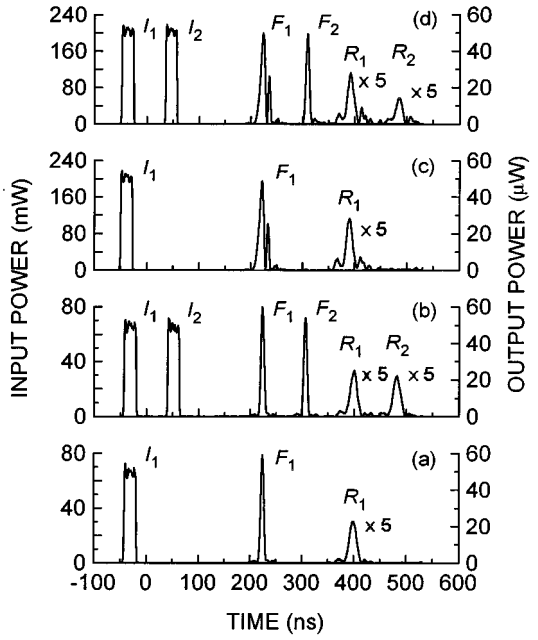

FIG. 8. Representative high-power pulse profiles for the single- and double-pulse experiments in the backward volume wave configuration for the 5.1-μm-thick yttrium iron garnet film strip, a static magnetic field of 1384 Oe, and a carrier frequency of 5.779 GHz. (a) Input and output soliton pulse signals vs time for the single-pulse experiment from Fig. 3. (b) Input and output soliton pulse signals vs time for the two-pulse experiment from Fig. 3. (c) Input and output pulse signals vs time for the single-pulse experiment and a power level well above the level required for solitons. (d) Input and output soliton pulse signals vs time for the two-pulse experiment and a power level well above the level required for solitons. The nominal position of the output transducer relative to the input transducer was 6.6 mm. The nominal spacing between the output transducer and the reflecting film edge was 2.2 mm.

main peak. Note also that the amplitude of the main peak is smaller than the corresponding peak in Figs. 8(a) or 8(b), even though the power level is higher by a factor of 3. This turnover effect in the main peak amplitude is characteristic of the situation which occurs when higher-order solitons are generated.[7,8] The reflected R_1 pulse in Fig. 8(c) is also changed in relation to the F_1 pulse. In contrast to the situation in Fig. 8(a), the R_1 pulse in Fig. 8(c) does not have the same shape as the F_1 pulse. Presumably, this is due to the decay which occurs during the return trip prior to the second detection and a corresponding drop in amplitude below the order 2 soliton threshold. Note that the R_1 pulse in Fig. 8(c) is similar in amplitude to the R_1 pulse in Fig. 8(a) but has a somewhat more complicated shape.

The interesting effects occur for two pulses and powers well above the single-soliton threshold, as shown in Fig. 8(d). Perhaps the most interesting effect is for the forward traveling pulses. The F_1 pulse in Fig. 8(d) is identical to the F_1 pulse in Fig. 8(c). However, the second forward traveling pulse, the F_2 pulse, is now changed significantly. Note that these two pulses are launched approximately 85 ns apart. One would expect, in principle, that the first pulse would have no effect on the second pulse. While this expectation is valid at low powers and even for solitons at moderate power

levels, it does not appear to be true at higher powers. It is clear from the shapes of the F_1 and F_2 pulses in Fig. 8(d) that the first pulse must produce some sort of a wake which affects significantly the evolution of the second pulse prior to detection.

Turn now to the effects of collision, as shown by the R_1 and R_2 pulses in Fig. 8(d). The initial pulse shape after the return trip is about the same as in the case of one pulse only and no collision. The R_1 pulse in Fig. 8(d) has the same profile as the R_1 pulse in Fig. 8(c). The R_2 pulse, however, is quite different. The most obvious effect is a decrease in peak power by a factor of 2 or so, relative to the peak power for R_1 pulse. This factor of 2 drop occurs in spite of the fact that the F_2 pulse has about the same peak value as the F_1 pulse.

The above results indicate that the effects of collision between nonlinear MME pulse signals at power levels above those for single solitons is quite complicated. The above results are presented here simply as a matter of experimental fact. It is clear that further experiments and extensive theoretical modeling will be needed to further define and understand these effects.

V. SUMMARY AND CONCLUSION

The work reported above demonstrates several new aspects of soliton physics in general and MME solitons in magnetic films in particular.

The data on pulse decay during propagation and reflection demonstrate clear regimes for soliton formation, propagation, decay, and changeover back to linear MME wave packets. The details of the pulse amplitude decay before and after reflection from the end edge of the supporting film reveal a useful power pickoff effect as the pulse moves over the pickup transducer. This effect allows one to determine experimentally the absolute power associated with the soliton MME pulse. These experimentally determined soliton peak powers and measured soliton widths, while consistent with predictions for simple sech-type order one soliton pulse, exhibit some significant departures from the simple theory.

The follow-on and collision properties when two separate MME pulses are propagated at powers in the single-soliton regime and at somewhat higher powers demonstrate several new effects. Solitons at power levels just above threshold behave as expected. These pulses pass through each other without appreciable change. However, there are new and unexpected effects at higher powers. First, there is a wake effect in which the shape of a second soliton following behind a previously launched soliton is significantly modified. Second, there is a collision effect, in which the second soliton suffers a significant additional decay.

Further work is needed for both the one-pulse and the two-pulse scenarios. For single pulses, careful measurements are needed to clarify group velocity discrepancies found for different power levels and opposite propagation directions and to better define the amplitude-width relations for order one solitons. For double pulses, it is necessary to quantify the wake and interaction properties observed at high power.

ACKNOWLEDGMENTS

The authors gratefully acknowledge Professor Pavel Kabos and Professor Andrei N. Slavin, Dr. Michael A. Wittenauer, Dr. Michael J. Hurben, and Dr. Hua Xia, and Harold E. Ensle for helpful discussions. This work was supported in part by the North Atlantic Treaty Organization (NATO) International Scientific Exchange Linkage Grant Program, Grant No. HTECH.LG 931489, the Russian Foundation for Basic Research, Grant No. 96-02-19515, the International Science Foundation and Russian Government, Grant No. R3E 300, the National Science Foundation, Grant No. DMR-9400276, and the U.S. Army Research Office, Grant Nos. DAAL03-91-G-0327 and DAAH04-95-1-0325.

[1] M. J. Ablowitz and H. Segur, *Solitons and the Inverse Scattering Transformation* (SIAM, Philadelphia, 1981).

[2] G. L. Lamb, *Elements of Soliton Theory* (Wiley, New York, 1980).

[3] R. K. Dodd, J. C. Eilbeck, J. D. Gibbon, and H. C. Morris, *Solitons and Nonlinear Wave Equations* (Academic, London, 1982).

[4] G. P. Agrawal, *Nonlinear Fiber Optics* (Academic, Boston, 1989).

[5] B. A. Kalinikos, N. G. Kovshikov, and A. N. Slavin, Zh. Eksp. Teor. Fiz. **94**, 159 (1988) [Sov. Phys. JETP **67**, 303 (1988)].

[6] B. A. Kalinikos, N. G. Kovshikov, and A. N. Slavin, Phys. Rev. B **42**, 8658 (1990).

[7] M. A. Tsankov, M. Chen, and C. E. Patton, J. Appl. Phys. **76**, 4274 (1994).

[8] M. Chen, M. A. Tsankov, J. M. Nash, and C. E. Patton, Phys. Rev. B **49**, 12 773 (1994).

[9] B. A. Kalinikos, N. G. Kovshikov, P. A. Kolodin, and A. N. Slavin, Solid State Commun. **74**, 989 (1990).

[10] M. Chen, M. A. Tsankov, J. M. Nash, and C. E. Patton, Phys. Rev. Lett. **70**, 1707 (1993).

[11] B. A. Kalinikos and N. G. Kovshikov, Pis'ma Zh. Eksp. Teor. Fiz. **60**, 290 (1994) [JETP Lett. **60**, 305 (1994)].

[12] R. W. Damon and J. R. Eshbach, J. Phys. Chem. Solids **19**, 308 (1961).

[13] V. F. Dmitriev, B. A. Kalinikos, and N. G. Kovshikov, Zh. Techn. Fiz. **56**, 2169 (1986) [Sov. Phys. Tech. Phys. **31**, 1300 (1986)].

[14] M. J. Hurben and C. E. Patton, J. Magn. Magn. Mater. **139**, 263 (1995).

[15] A. K. Zvezdin and A. F. Popkov, Zh. Eksp. Teor. Fiz. **84**, 606 (1983) [Sov. Phys. JETP **57**, 350 (1983)].

[16] B. A. Kalinikos, N. G. Kovshikov, and A. N. Slavin, IEEE Trans. Magn. **28**, 3207 (1992).

[17] V. F. Dmitriev and B. A. Kalinikos, Izv. Vyssh. Uchebn. Zaved. Fiz. **31**, 24 (1988) [Sov. Phys. **31**, 875 (1988)].

[18] B. A. Kalinikos, N. G. Kovshikov, and A. N. Slavin, Fiz. Tverd. Tela **27**, 226 (1985) [Sov. Phys. Solid State **27**, 135 (1985)].

[19] J. M. Nash, C. E. Patton, and P. Kabos, Phys. Rev. B **51**, 15 079 (1995).